ELSEVIER

Contents lists available at ScienceDirect

International Journal of Mechanical Sciences

journal homepage: www.elsevier.com/locate/ijmecsci





Abnormal crack coalescence and ductility in graphene

Suyeong Jin a, Jung-Wuk Hong b, Chiara Daraio b, Alexandre F. Fonseca c,d, Alexandre F. Fonseca

- ^a Department of Mechanical Engineering, Pukyong National University, 45 Yongso-ro, Nam-gu, Busan 48513, Republic of Korea
- ^b Department of Civil and Environmental Engineering, Korea Advanced Institute of Science and Technology, 291 Daehak-ro, Yuseong-gu, Daejeon 34141, Republic of Korea
- ^c Division of Engineering and Applied Science, California Institute of Technology, Pasadena, CA 91125, USA
- d Universidade Estadual de Campinas, Instituto de Física Gleb Wataghin, Departamento de Física Aplicada, 13083-859, Campinas, SP, Brazil

ARTICLE INFO

Keywords: Graphene design Parallel cracks Crack coalescence Fracture Stress intensity factor

ABSTRACT

Crack coalescence is a critical component in the study of mechanical resistance and the stability of materials. In the particular case of graphene, despite the extensive investigation of the formation and behavior of individual cracks in graphene, the study of crack coalescence within its structure remains unexplored. In this study, we investigate the interaction between two preexisting cracks and their effect on the mechanical properties of graphene using molecular dynamics simulations. The behavior of zigzag and armchair graphene structures with cracks separated by distances ($W_{\rm gap}$) is analyzed under tensile loading. The findings reveal that crack coalescence, defined as the formation of a new crack from two existing crack tips, occurs for lower values of the distance between cracks, $W_{\rm gap}$, resulting in a decline in the strength of structures. As $W_{\rm gap}$ increases, the stress-strain curves shift upward, with the peak stress rising in the absence of crack coalescence. The effective stress intensity factor formulated in this study exhibits a clear upward trend with increasing W_{oan} . Furthermore, an increase in $W_{\rm gap}$ induces a transition in fracture behavior from crack coalescence to independent propagation with intercrack undulation. This shift in fracture behavior demonstrates a brittle-to-ductile transition, as evidenced by increased energy absorption and delayed failure. A design guideline for the initial crack geometry is suggested by correlating peak stress with $W_{\rm gap}$, within a certain range. The findings offer insights into the fracture mechanics of graphene, emphasizing the impact of crack interaction and geometry on strength. This provides design guidelines for graphene-based structures with enhanced mechanical performance.

1. Introduction

Graphene is a promising material for various electrical, thermal, and mechanical applications because of its exceptional physical properties [1–4]. With a Young's modulus of 1 TPa and an intrinsic strength of 130 GPa [5], pristine graphene became the paradigm of a lightweight material with remarkable mechanical properties. Despite these outstanding properties, the development of large scale applications is still facing significant challenges in both the growth of large-area perfect graphene and its transfer without damages to any kind of substrate.

In fact, the production of large-area graphene has been possible for more than a decade through chemical vapor deposition (CVD) method [6]. This technique exploits the low solubility of carbon in metals such as copper [7] and nickel [8] to facilitate graphene growth on metallic foils. Despite its popularity and widespread use, the CVD growth method has not yet produced graphene samples of consistent

quality and reproducibility [9,10]. Although one of these challenges is being surmounted (see, for example the recent report of Amontree et al. [11]), it still remains challenging to transfer as-grown graphene samples to different substrates without damaging them [10]. The transfer process can introduce imperfections, such as cracks and tears, into graphene films, which might affect their properties [12].

Notwithstanding the aforementioned challenges, it may be posited that the imperfections of graphene may not be as deleterious as initially presumed. For instance, graphene sheets with grain boundaries have been demonstrated to exhibit strength that is comparable to that of the pristine material [13]. The ultimate failure of nanocrystalline graphene with previous flaws was demonstrated to not necessarily initiate at the flaw [14]. Defects have been shown to potentially confine crack propagation in graphene [15], and dislocations have been found to be shielded on graphene nanocracks [16].

E-mail addresses: daraio@caltech.edu (C. Daraio), afonseca@ifi.unicamp.br (A.F. Fonseca).

^{*} Corresponding author.

^{**} Corresponding author at: Universidade Estadual de Campinas, Instituto de Física Gleb Wataghin, Departamento de Física Aplicada, 13083-859, Campinas, SP. Brazil.

The presence of cracks and other imperfections in graphene may lead to the emergence of novel and intriguing properties and applications. Mosterio and Fonseca [17] have demonstrated that the thermal expansion behavior of holes in graphene is opposite to that of holes in two-dimensional materials. Chen et al. [18] have reported a scalable process to produce "holey-graphene", i.e., few-layer graphene nanosheets that possess nanoscale holes. The presence of grain boundaries and vacancies in graphene has been demonstrated to reduce its thermal conductivity [19]. In contrast, studies have demonstrated that cracks and tears have a negligible effect on the electrical properties of graphene [20]. A combination of these last two results can be of interest in the development of new thermoelectric materials that require good electric conduction and low thermal conductivity [21].

While these and many other similar studies have contributed to the understanding of the mechanical properties of graphene with and without different kinds of defects and flaws, the study of interactions between different flaws in graphene remains much less explored. A few examples can be given. Dewapriya and collaborators [22-24] computationally simulated the interaction between crack and vacancies and/or holes, as well as boron-nitride inclusions in graphene. Yao et al. [25] have performed a similar study of nanoscale crack-hole interactions in chiral graphene nanoribbons. Inspired by an experimental work on asymmetric crack propagation in bidimensional polymeric materials containing sequences of cracks with a given geometry [26], Felix and Galvao [27] demonstrated through reactive molecular dynamics simulations the same rectification effect in crack propagation in graphene structures. These works demonstrated that the shape, size and position of the corresponding flaws have a significant impact on the enhancement of the mechanical properties of graphene.

In this study, the coalescence of two cracks and its effects on the fracture behavior of graphene are investigated as a function of crack gap. Computational tools of classical molecular dynamics (MD) with a known reactive force field are employed to simulate the application of tensile strains to the structures from the equilibrium to full rupture. Coalescence between cracks occurs during tensile loading in graphene samples when the crack gap is below a certain value, leading to deterioration in the material strength. However, above that value, the rupture of graphene displays ductile behavior, demonstrated by energy absorption and the fracture pattern. Since ductile behavior in graphene has been ruled out at any temperature below the melting point [28], this last effect indicates that the understanding of how two or more topological defects interact within graphene can enable the design of brittle-to-ductile behavior in this structure.

This work is organized as follows. In Section 2, we present the models of graphene samples with previous cracks, the computational methods employed to investigate the crack coalescence in graphene, and the results of three preliminary tests needed to determine the best protocols for this research. In Section 3, the main results and discussion of the tensile strain numerical experiments are presented. The main conclusions of this study are presented in Section 4.

2. Computational models and methods

In this section, the description of the graphene structures and the geometry of the initial cracks proposed in this study is presented, along with the computational methods and protocols. A series of preliminary tests are presented to determine the optimal protocols for the simulations of crack coalescence and propagation. The primary results are presented in the subsequent section.

2.1. Graphene structures and the geometry of preexisting cracks

Graphene is a well-known structure formed by a network of sp² carbon atoms located at the vertices of a hexagonal lattice [2]. The atomic models of pristine graphene and graphene with single and multiple preexisting cracks are considered in this study, as shown in

Fig. 1. The graphene with a single crack has a crack length of $2a_0$ and a width of 2b, as shown in Fig. 1(b). The single crack is split into two parallel cracks separated by a distance $W_{\rm gap}$ to form graphene with parallel cracks, as shown in Fig. 1. The parallel cracks exhibit identical crack geometry, each crack with a crack length of $2a_1$ and a width of 2b. The crack length $2a_1$ is not exactly half of $2a_0$ due to the atomic structure. Both armchair (AC) and zigzag (ZZ) structures are prepared with the corresponding patterns along crack boundaries. The dimensions of the structures are approximately 15 nm in width and length. The geometry of the single crack and two parallel cracks are listed as in Table 1. Given that sample size might affect the stress–strain response, all simulated structures are designed to be sufficiently larger than the crack dimensions and the distances between adjacent cracks, minimizing size effects. The boundaries of all structures along the ydirection are passivated by hydrogen, as well as the internal boundaries of the cracks.

The tensile test is simulated on the graphene structures by applying tensile strain along the x-direction. This study investigates the influence of crack gap $W_{\rm gap}$ on the mechanical properties and fracture behavior of the graphene structure. Pristine graphene and graphene with a single crack, each with armchair and zigzag orientations, are used as reference cases. The simulations will encompass a total of 16 structures with the crack geometry, as listed in Table 1.

2.2. Computational methods and protocols

In this subsection, the computational methodologies and protocols that were utilized in our simulations are delineated. First, the choice of force field that could best describe the physical and chemical properties of crack propagation and coalescence in graphene will be discussed. Subsequently, an analysis is conducted to identify the most suitable boundary conditions for the graphene structures in the simulations. This analysis is undertaken to ensure that the dynamics and behaviors of the cracks are minimally influenced by any effects arising from the imposed boundary conditions. This subsection also presents the details about the molecular dynamics protocols of all simulations.

2.2.1. Choice of force field

Molecular dynamics (MD) simulations will be performed using the computational tools of the LAMMPS package [29]. The reactive force field (ReaxFF) potential [30] will be used to model the interaction between carbon-carbon and carbon-hydrogen atoms. Despite the extensive utilization of the "adaptive intermolecular reactive empirical bond order (AIREBO)" potential [31,32] in the study of the mechanical and thermal properties of carbon nanostructures [13,33–37], including crack propagation and fracture of graphene [3,14,27,38-47], concerns regarding the reliability of AIREBO in accurately simulating carboncarbon bond breaking have been documented, even when accounting for a specific adjustment to the *cutoff* parameter of the potential [48]. As the objective of this investigation is not to provide a comparison to the results of the aforementioned studies, we opted to select a force field that may prove more effective in dealing with the breaking of carbon-carbon bonds and reactions to study the crack coalescence in graphene.

ReaxFF was developed to enable more precise simulations of chemical reactions, including bond breaking and formation [30]. Consequently, it is an optimal choice of force field for the present study of the coalescence phenomenon of cracks in graphene. Indeed, ReaxFF has been employed to effectively simulate the full stress–strain relationship of several one-dimensional [49–53] and two-dimensional (2D) [54–56] nanomaterials.

The ReaxFF set of parameters derived to simulate combustion in carbon, hydrogen and oxygen (C-H-O) systems, developed by Chenoweth et al. [57], was selected for use. This set of parameters is included with the standard distribution of LAMMPS and has been employed, for example, to study the mechanical and fracture properties of graphene oxide structures [58–60] and graphyne [61].

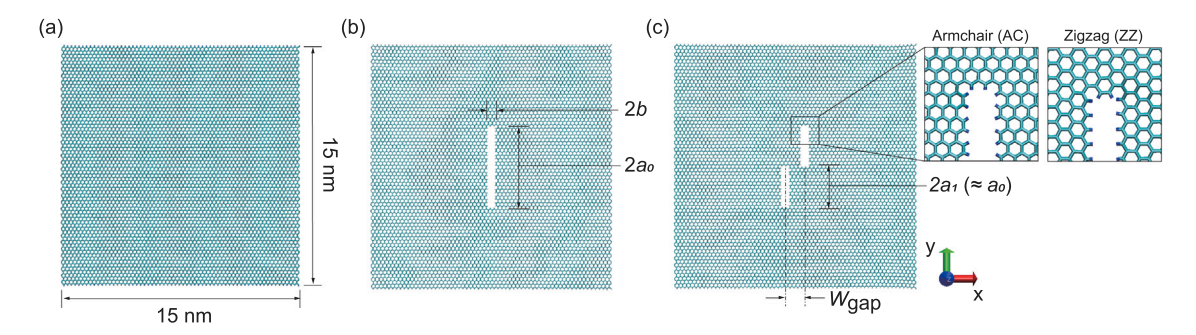


Fig. 1. Geometry and structure of graphene structures studied here. (a) pristine graphene, (b) graphene with a single crack of length $2a_0$ and width 2b, and (c) graphene with two cracks, each of length $2a_1$ and width 2b, separated by a distance W_{gap} . A magnified view of a portion of the crack is provided to show its local structure. Cyan (blue) represents carbon (hydrogen) atoms in the structure.

Table 1 Graphene structures featuring preexisting cracks, as shown in Fig. 1. The labels "AC" and "ZZ" denote armchair and zigzag chiralities, respectively, and the following digit indicates the case number. Cases AC1, AC6, ZZ1, and ZZ6 have no $2a_1$ because they are structures with a single crack, representing $W_{\rm gap} = 0$.

Case	2a ₀ (nm)	2 <i>a</i> ₁ (nm)	2b (nm)	$W_{\rm gap}$ (nm)	Case	2a ₀ (nm)	2a ₁ (nm)	2b (nm)	$W_{\rm gap}$ (nm)
AC1	5.388	_	0.614	0	ZZ1	5.281	_	0.567	0
AC2	-	2.836	0.614	1.228	ZZ2	-	2.825	0.567	1.276
AC3	-	2.836	0.614	1.719	ZZ3	-	2.825	0.567	1.701
AC4	-	2.836	0.614	2.947	ZZ4	-	2.825	0.567	2.978
AC5	-	2.836	0.614	4.175	ZZ5	-	2.825	0.567	4.254
AC6	2.411	-	0.614	0	ZZ6	2.333	_	0.567	0
AC7	-	1.347	0.614	1.719	ZZ7	-	1.351	0.567	1.701
AC8	-	1.347	0.614	4.175	ZZ8	-	1.351	0.567	4.254

2.2.2. MD methods I: boundary conditions

The tensile simulations are performed without periodic boundary conditions. Dirichlet boundary conditions are imposed on two narrow regions at the leftmost and rightmost vertical edges of the structure, each with a width of 2.4 Å. The region on the left is kept fixed in the x-direction, while the region on the right is made to move at a constant velocity. This represents the external application of strain at a constant strain rate. This approach eliminates the need for barostatting algorithms, which require the correct use of damping factors [62] and demand extensive simulation times.

Two distinct types of Dirichlet boundary conditions are tested on representative samples to determine the most appropriate tensile-strain application protocol for this study. The first type of boundary condition involves fully constraining the atoms in the left region and applying a constant velocity in the x-direction to the atoms in the right region, while fixing their y- and z-coordinates. This type is referred to as "Fixed BC" (where BC denotes boundary conditions). The second type consists of fixing only the x-coordinate of the atoms in the left region, while allowing their *y*- and *z*-coordinates to move based on interactions between them and the atoms in the rest of the structure. The atoms in the right region are moved at a constant x-coordinate velocity. This type is referred to as "Free BC". Simulations of the full tensile stressstrain of two structures (one pristine and one precracked graphene) are performed for each type of BC to determine which type is best for our study. In these tests, the structures are stretched along the *x*-direction by appropriately choosing the value of the x-coordinate velocity, v_x , to represent the strain rate value of 10^7 s⁻¹.

2.2.3. MD methods II: main protocols

Three primary protocols are employed in the MD simulations. The first two are used to address the equilibration of structures at 0 K and $300 \, \text{K}$, respectively, while the third outlines the tensile strain numerical experiment.

In the first protocol, energy minimization is performed using the conjugate gradient algorithm to relax as-built atomic configurations shown in Fig. 1. The convergence criteria are set to 10^{-9} (dimensionless) for energy and 10^{-9} (kcal/mol)/Å for force. This initial step is essential for correcting atomic positions according to the force field.

In the second protocol, the structures are then equilibrated at 300 K using the following protocol. All dynamic simulations are performed with a timestep of 0.05 fs. A Langevin thermostat [63] is applied to all atoms of the structures except those located in the leftmost and rightmost regions, as defined in the previous subsection for the boundary conditions. The target temperature and damping factor are set to 300 K and 5 fs, respectively. Atoms in the left and right boundary regions are constrained differently. For the atoms in these regions, their zcoordinates are kept fixed to resemble clamped boundaries, while their x- and y-coordinates are allowed to freely move in accordance with their interactions with the other atoms of the system. This equilibration protocol ensures full relaxation of the system, including thermal expansion effects that alleviate any residual thermal stresses. The equilibrium size along the x-direction, L_0 , is defined as the difference between the average x-coordinates of the atoms located in the right and left boundary regions.

The third protocol involves the numerical tensile strain experiment, where the conditions of the type of BC (Fixed or Free) are considered. In these simulations, the atoms on the left are kept fixed, while the atoms on the right are moved along the x-direction at the constant velocity given by

$$v_{x} = L_{0}\dot{\varepsilon} \,, \tag{1}$$

where $\dot{\varepsilon}$ is the strain rate.

LAMMPS calculates the stress tensor for every atom of the system according to the following formula:

$$\sigma_{ab} = m v_a v_b + W_{ab} \,, \tag{2}$$

where a and b represent any of the x, y or z coordinates, and W represents the virial contribution to the stress on one atom due to its interaction with N_p neighbors, through:

$$W_{ab} = \frac{1}{2} \sum_{j}^{N_p} \left(r_{1a} F_{1b} + r_{2b} F_{2a} \right) , \tag{3}$$

where \mathbf{r}_j (j = 1, 2) are the position vectors of a pair of interacting atoms with \mathbf{r}_j being the resultant force on atom j.

The total stress along x-direction is, therefore, computed from the summation of the x-component of the stresses, σ_{xx} (i.e., setting a = b = x in Eq. (2)), of all carbon atoms but those at the edge regions of the system. Similar for the stresses along y and z directions.

In order to get a qualitative picture of the local stresses on the structure during the tensile test, we computed the von Mises [64] stress per atom, σ_{vm} . It is given by:

$$\sigma_{\text{vm}} = \sqrt{0.5 \left[(\sigma_{xx} - \sigma_{yy})^2 + (\sigma_{yy} - \sigma_{zz})^2 + (\sigma_{zz} - \sigma_{xx})^2 + 6(\sigma_{xy}^2 + \sigma_{yz}^2 + \sigma_{zx}^2) \right]},$$
(4

with σ_{ab} of every atom calculated from Eq. (2).

The total stress and strain values of the system are exported every 500 timesteps, while the frames corresponding to the structure under the tensile strain experiment are exported every 0.5% strain.

A critical issue regarding the stress calculations in LAMMPS should be discussed. As the volume of an atom is not a well-defined quantity, the LAMMPS algorithms that calculate the stress per atom express it in units of [stress.volume]. To obtain values of stresses and other mechanical quantities related to the stress–strain curve in units of stress, the volume of the whole system must be calculated or, at least, estimated. In the case of one-atom thick structures such as graphene, the longitudinal, L_x , and transversal, L_y , dimensions are relatively well defined, while the thickness, t, is usually taken as equal to the distance between layers in graphite. Consequently, to calculate the stresses of a graphene sample, it suffices to calculate its volume by simply multiplying $L_x L_y t$. This method for obtaining the stresses from the above LAMMPS computation is referred to here as the "common method".

In this study, the structures under consideration are not homogeneous two-dimensional (2D) systems. They contain holes, and as displayed in the Results section, the tensile strain generates multiple undulations and partial ruptures within the systems. The volume of these structures cannot be anymore accurately represented as the product of the longitudinal, transversal, and thickness dimensions. Consequently, rather than utilizing the external dimensions of our structures to compute their volumes, we opted to employ another LAMMPS algorithm that computes the Voronoi tessellation of the atomic system. This approach provides an estimate of the volume per atom for each system. However, as this method is not commonly employed in the study of stress–strain behavior in 2D materials, it is imperative to ascertain whether this approach under- or overestimates the volume of the system. This will have a direct impact on the values of stresses.

The verification of the effect of the volume calculation by the Voronoi method on the stresses of our structures is conducted as follows. We have simulated the stress–strain relation of a few samples within only the linear elastic regime, where we are certain that the volume of the structure can be simply calculated by $L_x L_y t$. Pristine graphene and graphene with two cracks with $W_{\rm gap}=0$ samples were chosen for this test. In the case of graphene with the cracks, due to their rectangular shape, its volume can be simply calculated by $l_x l_y t$, where l_x and l_y are the lateral sizes of the crack, and subtracted of the total volume of the sample. Then, we compare the values of the elastic moduli obtained from both methods. As demonstrated in the subsequent subsection, these values are not in agreement. Therefore, a correction factor, c, was defined to be further applied to all stress calculations with the Voronoi method.

Summarizing, since the Voronoi method can more precisely capture the volume of the deformed shape of tensile-strained structures, it was used in all simulations. As this method overestimates (as shown in the next subsection) the calculation of the volume, the parameter c is used to correct the stress values. The numerical parameters used in the simulations are presented in Table 2.

Table 2
Parameters of all MD simulations.

Parameter	Value
Convergence criteria for energy	10 ⁻⁹ (dimensionless)
Convergence criteria for force	10 ^{−9} (kcal/mol)/Å
Temperature	300 K
Timestep	0.05 fs
Thermostat	Langevin [63]
Temperature damping factor	5 fs
Interval of exporting stress - strain values	25 fs
Interval of exporting structure frames	Every 0.5% strain

2.3. Simulation tests

In order to ascertain the most optimal conditions for executing all simulations in the present study, three tests were conducted. The first test pertained to ascertaining the most suitable type of boundary condition (BC). The second test focuses on the effects of the strain rate, $\dot{\epsilon}$, and involves conducting MD simulations of the full tensile stress–strain of a pristine structure and a precracked structure at three distinct values of $\dot{\epsilon}$: 10^9 , 10^8 , and 10^7 s⁻¹. The third test was designed to determine the parameter c (defined in the previous section) to correct the values of the stresses and elastic moduli due to the use of the Voronoi method to calculate the volume of the structures. The ensuing subsections will present the outcomes of these tests.

2.3.1. Boundary condition test

The two types of Dirichlet BC conditions mentioned in Section 2.2.2 were applied to AC graphene samples with and without initial cracks, as shown in Fig. 1, to investigate the boundary effect and identify the most suitable condition for subsequent simulations. For this test, the crack gap $W_{\rm gap}$ is set to 0.614 nm, equivalent to approximately four times the width of the graphene regions at the edges. The strain rate used for this test is $10^7~{\rm s}^{-1}$. The Voronoi method was used to determine the volume of the system during the tensile strain simulations.

Fig. 2 allows us to infer the main results of this test. The first two rows show the pristine and precracked graphene structures, respectively, at about 7% of strain, for fixed (left column) and free (right column) BCs. Different colors within the structures represent the normalized local von Mises stresses whose color scale is given on the right of the figures. The stress is normalized by the certain value to maximize the visualization. Every structure shows a magnification of one of its corners in order to highlight the local deformation of the atomic structure due to the type of BC. The fixed BC generates stresses and strains on the atoms at the corners of the structures with high transversal components. Some chemical bonds are broken or close to be broken. It prematurely transmits stresses to the regions containing the cracks (compare left and right columns of Fig. 2b). Free BC does not generate the same stresses at the edges, so the applied tensile strain concentrates more uniformly around the cracks. Notice that, at the same strain, the atoms at the edges are not broken yet.

The free BC constraint enables structures to fully relax along the transversal direction, resulting in more uniform Poisson's effect, i.e., more uniform transversal edges during the application of tensile strain compared to structures simulated under fixed BCs. This resembles the observations in tensile strain simulations performed under transversal periodic boundary conditions, where barostat algorithms are used to relax the system along the transversal directions. In contrast, the fixed BC generates a "U"-shaped curve at the transversal edges. This effect would likely be negligible for larger structures. However, larger structures would require significantly more computational resources. Therefore, the free BC was employed in the simulations of the tensile strain for all other structures.

Fig. 2(c) presents the stress-strain curves of graphene structures with and without cracks, from both fixed and free BCs. In the case of

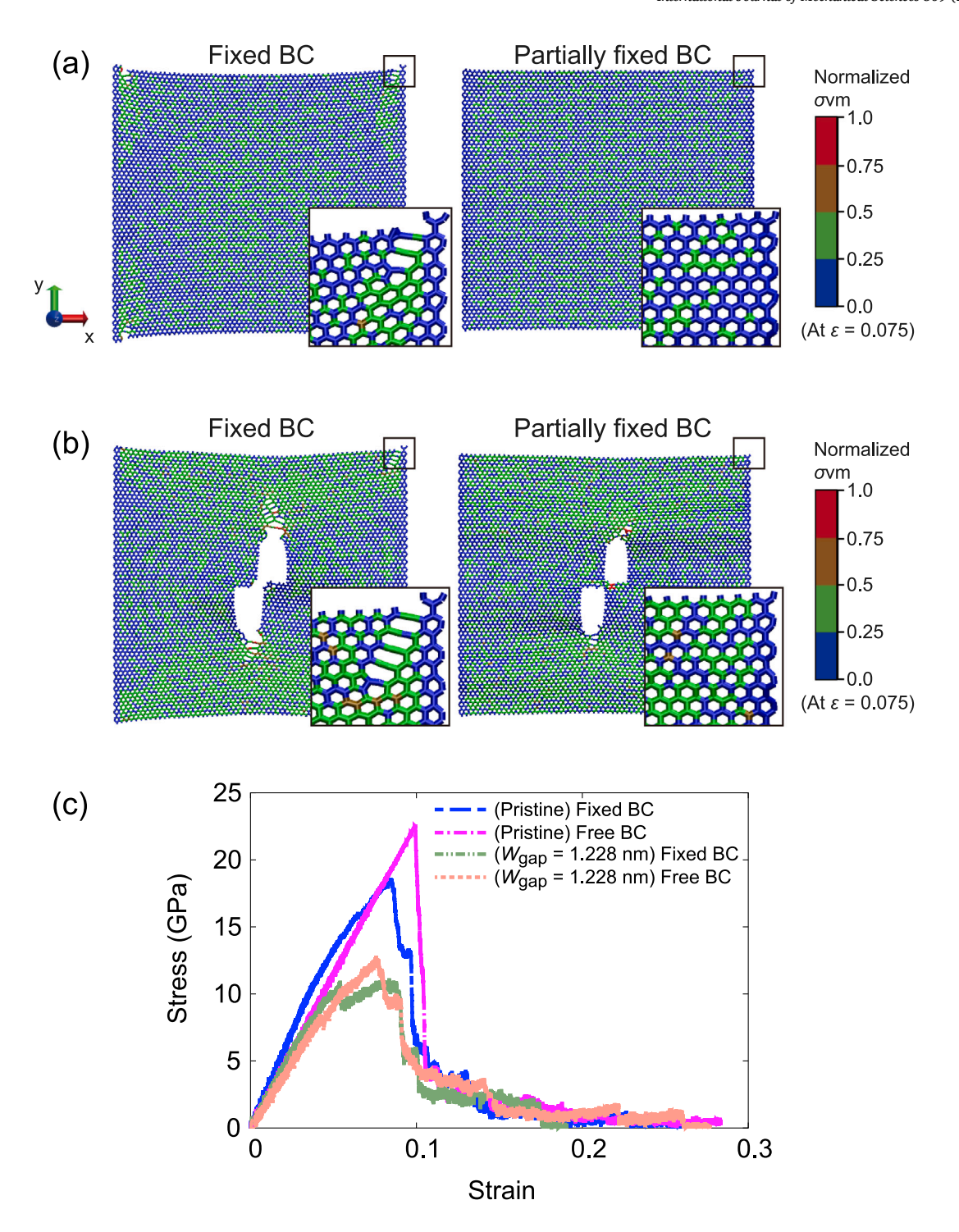


Fig. 2. Effects of boundary conditions in tensile MD simulations of monolayer graphene with and without initial cracks at strain rate of 10^7 /s. Normalized von Mises stress distribution under a tensile strain of 0.06 for (a) pristine graphene and (b) precracked graphene. (c) Stress–strain curves. The correction for the stress values due to the use of Voronoi method was not applied here.

precracked structures, although the stress–strain curves are not significantly different when comparing fixed and free BCs, a slight difference is observed in the inclination of the linear region and in the maximum stress value. However, a more pronounced difference is observed in the stress–strain curves of pristine graphene when comparing fixed and free BCs. In addition to the inclinations of the linear regions of both curves

being visibly different, the values of peak stress and tensile strain at break are also significantly different.

Summarizing, our conclusion here is that the free BC minimizes the influence of boundary effects on the structure of the tensile-strained systems. In order to focus on the behavior in the cracked region, the free BC is selected for all additional simulations.

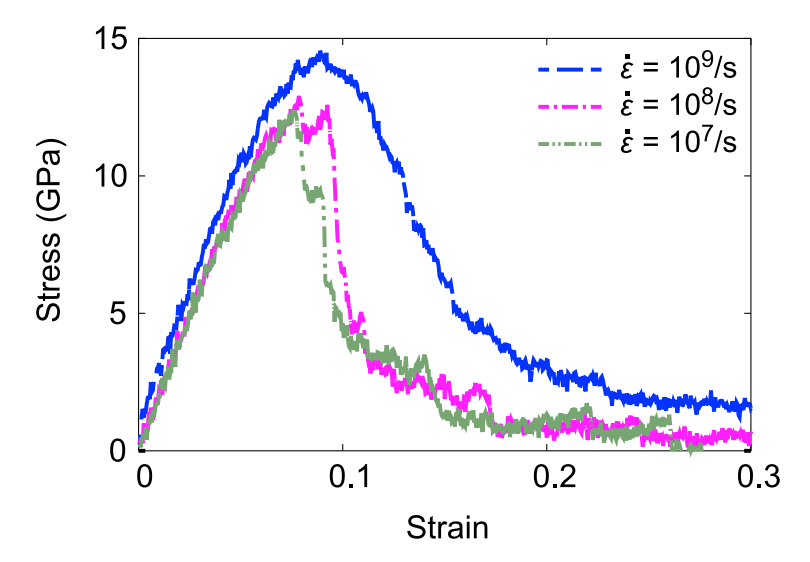


Fig. 3. Stress-strain curves for different strain rates for the precracked graphene structure with $W_{\rm gap} = 1.228$ nm. The correction for the stress values due to the use of Voronoi method was not applied here.

2.3.2. Strain rate effect

The effect of the strain rate on the mechanical response of the system to tensile strain is investigated for graphene with initial cracks separated by $W_{\rm gap} = 1.228$ nm, as shown in Fig. 1. The crack surface is taken in the armchair direction. The strain rate, $\dot{\epsilon}$, values considered in this test are 10^7 s⁻¹, 10^8 s⁻¹, and 10^9 s⁻¹.

Fig. 3 shows the stress–strain curves at varying strain rates for the system under investigation. The primary observation is that while the peak stress increases with $\dot{\epsilon}$, it exhibits a substantial increase when the strain rate is varied from 10^8 s⁻¹ and 10^9 s⁻¹. Furthermore, it is evident that the responses at strain rates of 10^7 s⁻¹ and 10^8 s⁻¹ are similar. Specifically, the peak stress values of 12.92 GPa and 13.27 GPa are observed at strain rates of 10^7 s⁻¹ and 10^8 s⁻¹, respectively. The corresponding strain values of 0.0767 and 0.0790, recorded at these peak stress levels, are also very close. The difference in peak stress is -0.35 GPa, which corresponds to a -2.71% relative change. Therefore, as the results for strain rates of 10^7 s⁻¹ and 10^8 s⁻¹ are analogous, the former is selected for all subsequent fracture simulations. This approach is employed to reduce the time required for computational calculations while maintaining the physical significance of the data.

2.3.3. Volume correction

As previously explained, the stress per atom, as calculated by LAMMPS, requires the computation of the system's volume. As the holes undergo changes in shape and size during the tensile-strain numerical experiments, and the plastic regime of deformation causes undulations and partial bond breakings within the structure, the Voronoi tessellation method is chosen because it is capable of continuously estimating the volume of the system taking into account the various forms of deformations observed in the different structures. However, it is imperative to ascertain that this method does not under- or overestimate the volume, as this would adversely affect the stress values.

To accomplish this, tensile simulations of pristine and AC and ZZ graphene structures with $W_{\rm gap}=0$ were conducted, using the "common method" to estimate the volume. This method involves multiplying the dimensions of the structure to find its volume, which is valid during the elastic regime. Therefore, these tensile simulations will be performed only for up to 2.5% of strain. The Young's moduli of these structures are extracted and compared to those from the simulations where the Voronoi method was used to calculate the system's volume.

Fig. 4 shows the stress-strain curves of the tensile strain simulations for the structures mentioned above calculated using the Voronoi and

common volume methods. It is evident that the relationship between stress and strain is contingent on the method utilized for volume calculation. Specifically, it was determined that the Young's moduli obtained using the Voronoi volume method are approximately six times smaller than those obtained using the common volume method, as indicated in Table 3. Given the widely accepted value of 1 TPa for the Young's modulus of graphene [5], it can be concluded that the common volume method accurately measures the stress values, at least at the linear regime. Therefore, we define the factor \boldsymbol{c} as the ratio of Young's modulus obtained by using the common volume method to that using the Voronoi volume method.

In summary, the above tests allow us to determine the factor c to correct the stress values of all structures. So, from now on, the stress-strain curves and all results derived from them will be shown using the application of the average values of the factor, c=6.067, obtained based on Table 3.

3. Results and discussion

Tensile simulations are performed on graphene structures with pre-existing cracks separated by $W_{\rm gap}$, as described in Section 2.1, with the protocols and conditions detailed in Sections 2.2 and 2.3, respectively. In Section 3.1, the main results of the simulations are presented and discussed. In Section 3.2, a new model to describe the effects of the sizes of the parallel cracks on the peak stresses of the structures is presented and discussed. In Section 3.3, a more quantitative and detailed discussion about the fracture behavior is presented. From now on, the stress values shown in the figures are corrected for by the factor c.

3.1. Main results

The stress–strain curves for all values of $W_{\rm gap}$ are presented in Figs. 5(a) and (b) for the armchair and zigzag structures, respectively. For these results, the armchair structures use crack lengths of $2a_0=5.388$ nm and $2a_1=2.836$ nm (AC1 to 5), while the zigzag structures use $2a_0=5.281$ nm and $2a_1=2.825$ nm (ZZ1 to 5). In general, the curves for different values of $W_{\rm gap}$ are very similar, although the differences are more pronounced for ZZ structures than for AC ones. The area under the curves also looks similar, with a perceived tendency to increase with $W_{\rm gap}$. Although not exactly the same, the linear region of the stress–strain curves is also quite similar, indicating that the cracks did not significantly affect the order of magnitude of the elastic modulus of the

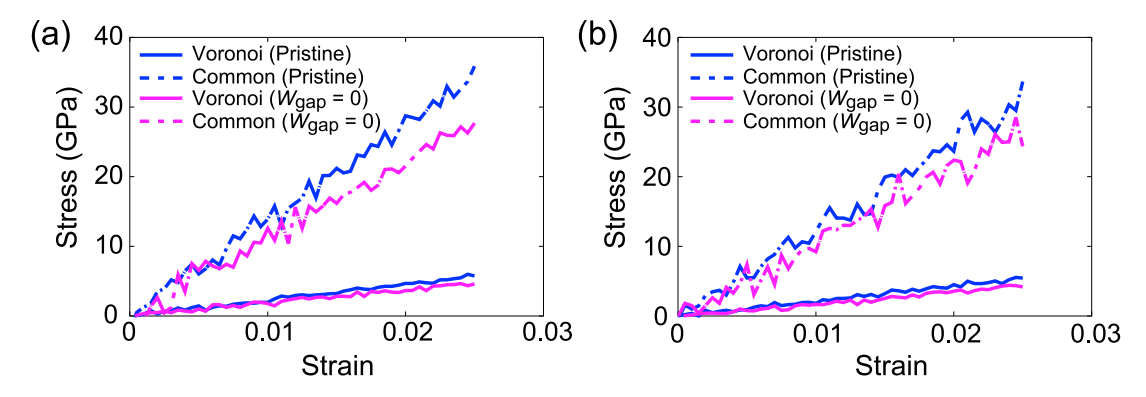


Fig. 4. Comparisons of stress versus strain curves at the linear elastic regime, obtained by using Voronoi (solid line) and Common (dashed line) volume methods. (a) Armchair and (b) zigzag structures. Pristine graphene (blue curves) and the graphene with the initial crack ($W_{\rm gap} = 0$, magenta curves) are examined for both structures.

Table 3 Correction factor c obtained from the simulations of pristine and $W_{\rm gap}=0$ structures, at different strain rate values, $\dot{\epsilon}_1$ using both Voronoi and common methods to calculate the volume of system.

Type	Structure	$\dot{\varepsilon}$ (s ⁻¹)	Volume method	Young's modulus (TPa)	Factor c	
Armchair	Pristine	10 ⁷	Common	1.339	6.032	
			Voronoi	0.222		
Armchair	$W_{\rm gap} = 0$	10 ⁷	Common	1.079	5.994	
			Voronoi	0.180	0.551	
Zigzag	Pristine	107	Common	1.268	6.126	
			Voronoi	0.207	0.120	
Zigzag	$W_{\rm gap} = 0$	107	Common	1.025	5,959	
			Voronoi	0.172	5.757	

structures. This is confirmed by the data shown in Fig. 5(c). The stress-strain curves clearly show an upward shift with increasing $W_{\rm gap}$. After the first major drop in stress, which occurs at a strain value of about 0.1, the differences in the stress–strain curves increase even more with $W_{\rm gap}$.

More specifically, for AC structures, Fig. 5(a) shows that the stress-strain curves for $W_{\rm gap}=0,1.228$, and 1.791 nm exhibit a high degree of similarity, while the curves for $W_{\rm gap}=2.947$ and 4.175 nm demonstrate a visible upward shift. For strain values greater than 0.1, all the curves begin to diverge and shift upward. Fig. 5(b) shows that the stress-strain curves of ZZ structures shift upward with $W_{\rm gap}$, like the AC cases. In addition, the peak stresses in ZZ structures have been found to be lower than those in AC structures, which is consistent with the existing literature on the propensity for fracture along the zigzag direction in graphene [39,65]. Furthermore, the curves of ZZ structures exhibit a reduced degree of similarity between themselves as compared to those of AC structures. Such deviation can be attributed to the aforementioned propensity for fracture along the zigzag direction, in conjunction with local intercrack structure characteristics, a subject that will be examined in Section 3.3.

The Young's modulus of the structures, calculated from the initial response to the strain of 0.01, increases with $W_{\rm gap}$, as shown in Fig. 5(c). When compared with the Young's modulus of pristine graphene, cracks reduce the Young's modulus of graphene with defects, as expected.

The peak stress increases with $W_{\rm gap}$, as shown in Fig. 5(d). A quantity directly related to the peak stress is the critical stress intensity factor, $K_{\rm IC}^{\rm eff}$. Its concept is well defined in the context of continuum mechanics, and is related to the fracture toughness of the materials. Nevertheless, it can be explored in conjunction with atomistic simulations to characterize the fracture of graphene. The effective stress intensity factor in mode-I is defined as

$$K_{\rm I}^{\rm eff} = \sigma \sqrt{\pi a^{\rm eff}},$$
 (5)

where σ is the stress, and $a^{\rm eff}$ is the effective crack length calculated as

$$a^{\text{eff}} = \begin{cases} a_0, & \text{(single crack),} \\ 2a_1, & \text{(parallel cracks).} \end{cases}$$
 (6)

Here, the effective stress intensity factor using a_0 is actually identical to the stress intensity factor. This expression can approximate the fracture toughness of the graphene structure with parallel multiple cracks. The effective critical stress intensity factor $K_{\rm IC}^{\rm eff}$ is, then, obtained by setting $\sigma=\sigma^p$, where σ^p is the peak stress of a stress–strain curve. Fig. 5(d) shows the effective critical stress intensity factor, $K_{\rm IC}^{\rm eff}$, with increasing $W_{\rm gap}$. Our values are within the range of the critical stress intensity factors of graphene obtained from computational and experimental data, from 3.4 to 12.0 MPa \sqrt{m} [66,67].

The energy absorption under the stress–strain curve is also calculated, as shown in Fig. 5(e). It shows a general increasing trend of the energy absorption, for both AC and ZZ structures with $W_{\rm gap}$. AC structures are always more capable of absorbing energy than ZZ ones, and the difference decreases for approximately $W_{\rm gap} > 1.3$ nm. In conjunction with the structural frameworks depicted in Figs. 6 and 7, a correlation between the energy absorption curves in Fig. 5(e) and the brittle-to-ductile transition for both AC and ZZ structures, with the increasing $W_{\rm gap}$ values, will be discussed ahead.

Regarding the fracture behaviors of the structures, two important general results can be observed in Figs. 6 and 7. They show snapshots of armchair and zigzag structures, respectively, at strain values of 0, 0.075, 0.1 and a particular value, named " ϵ_i ", which is chosen to represent and illustrate the kind of fracture behavior of each structure. For armchair structures having $W_{\rm gap}=0,1.228,1.791,2.947$ and 4.175 nm, the chosen snapshots correspond to values of $\epsilon_i=0.28,0.12,0.16,0.225$ and 0.26, respectively. For zigzag structures having $W_{\rm gap}=0,1.276,1.701,2.978$ and 4.254 nm, the chosen snapshots correspond to values of $\epsilon_i=0.17,0.12,0.215,0.2$ and 0.2, respectively. The strain value of $\epsilon=0.075$ is selected for capture, as it corresponds

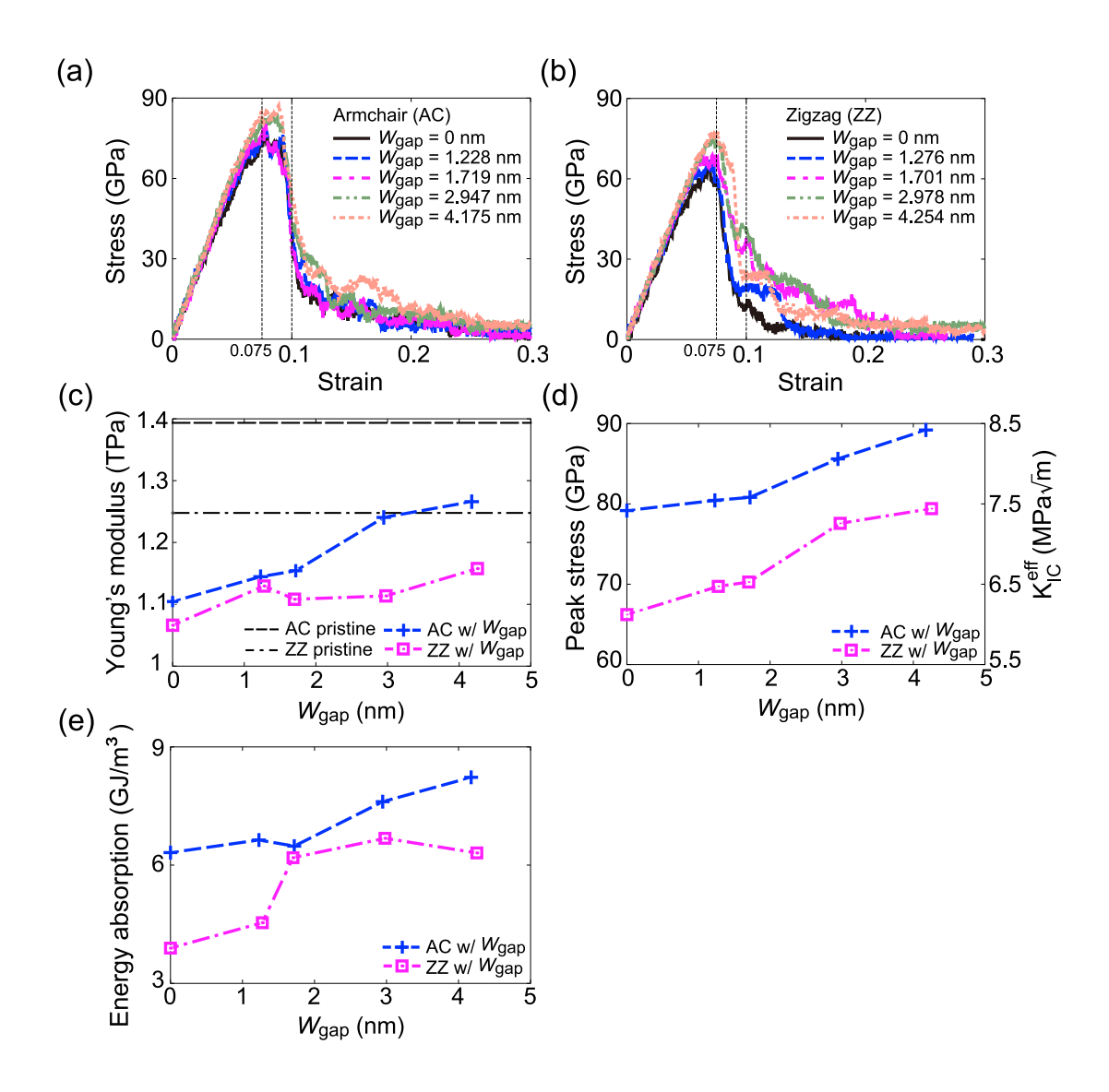


Fig. 5. Results of armchair (AC) structures with crack lengths of $2a_0 = 5.388$ nm and $2a_1 = 2.836$ nm (AC1 to 5), and zigzag (ZZ) structures with $2a_0 = 5.281$ nm and $2a_1 = 2.825$ nm (ZZ1 to 5). (a, b) Stress versus strain curves for armchair and zigzag, respectively, graphene structures with different values of $W_{\rm gap}$, at a strain rate of 10^8 s⁻¹. The vertical lines at strain values of 0.075 and 0.1 are references for the next two figures. (c) Young's modulus versus $W_{\rm gap}$ for both AC and ZZ structures. (d) Peak stress and effective stress intensity factor versus $W_{\rm gap}$, respectively, corresponding to the stress–strain curves shown in (a) and (b). (e) Energy absorption under the stress–strain curve. Lines are guides to the eye. See the legends for the different symbols and lines.

to the average of the strain values at peak stresses of the structures. The strain value $\varepsilon=0.1$ is chosen because, as shown in Figs. 5(a) and (b), at this value, the stress either rapidly dropped or is going to drop to nearly zero, and the structures are near fracture. It is also observed that the single crack propagates along the transverse direction in zigzag structures, and along the zigzag atomic directions in armchair ones, a feature better discussed in Section 3.3.

The first important result from Figs. 6 and 7 is that the coalescence of the cracks occurs only for the two smallest values of $W_{\rm gap}$, for both armchair and zigzag structures. The second important result regards an interesting behavior that emerges for the structures with the two largest values of $W_{\rm gap}$: for both armchair and zigzag patterns, the cracks do not coalesce. The region between the cracks, rather than merely being strained, begins to act as a flexible lever, causing the right side of the structure to move transversely with respect to the left side. This "lever"

type of fracture enables the system to withstand higher amounts of strain, which thereby exhibits ductile behavior. This phenomenon as well as the details regarding the evolution of the atomic structure of the region between the cracks during the tensile strain will be addressed in greater detail in the subsequent quantitative discussion of failure behaviors (Section 3.3).

The aforementioned characterization of the "lever" fracture type facilitates the discernment of a hallmark of the brittle-to-ductile transition in the findings presented in Fig. 5(e). It is possible to correlate this transition, in both AC and ZZ structures, with the behavior of the absorption energy curves in Fig. 5(e). For AC structures, the energy absorption curve starts increasing at a larger pace for $W_{\rm gap} \geq 2.947$ nm. For ZZ structures, the energy absorption curve suffers an abrupt increase for $W_{\rm gap}$ values between 1.276 and 1.701 nm. For AC structures, the "lever" fracture type happens for values of $W_{\rm gap} = 2.947$

Armchair

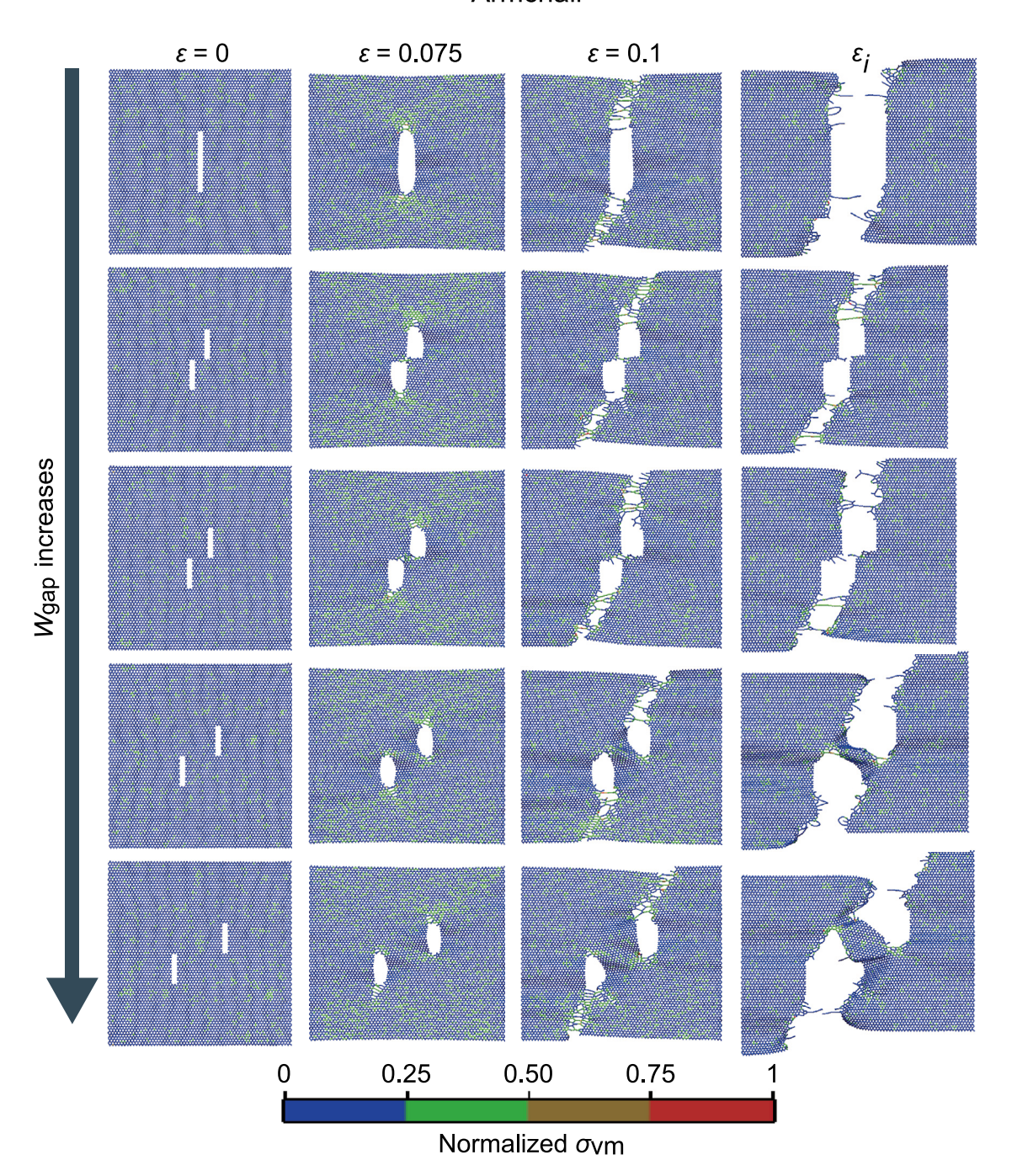


Fig. 6. Snapshots of the AC structures (AC1 to 5) at certain values of tensile strain. Rows display structures with increasing $W_{\rm gap}=0,1.228,1.719,2.947$, and 4.175 nm, from top to bottom. Columns display structures with strain values, from left to right, corresponding to $\varepsilon=0,0.075,0.1$ and a specific value named " ε_i ". This last one was chosen according to the fracture behavior of each structure. From top to bottom: $\varepsilon_i=0.28,0.12,0.16,0.225$ and 0.26. The color code corresponding to the scale of von Mises stresses, $\sigma_{\rm vm}$, is shown below the figures.

and 4.175 nm. For ZZ structures, the "lever" fracture type happens for values of $W_{\rm gap}=1.701,\,2.978,\,{\rm and}\,4.254$ nm.

It should be noted that the expression "brittle-to-ductile transition" used in this study denotes a relative change in fracture behavior rather than an intrinsic alteration of the material's fundamental brittleness. Graphene remains a brittle material at all temperatures [28]. Nevertheless, increasing $W_{\rm gap}$ modifies the local deformation and fracture sequence, resulting in a more ductile-like response characterized by higher rupture strain and enhanced energy absorption.

Furthermore, the interpretation of the results observed in Figs. 5(a) and 5(b) can be facilitated by the use of Figs. 6 and 7. The findings demonstrate that, for both AC and ZZ structures, the stress–strain curves attain their maximum values for the largest values of $W_{\rm gap}$. The underlying reason for this phenomenon can be deduced from the von Misses stress concentration within the structures for $\varepsilon=0.075$ (see second column in Figs. 6 and 7) The regions of the figure that are colored green indicate atoms that are experiencing greater levels of stress than the regions colored blue. It is observed that the common

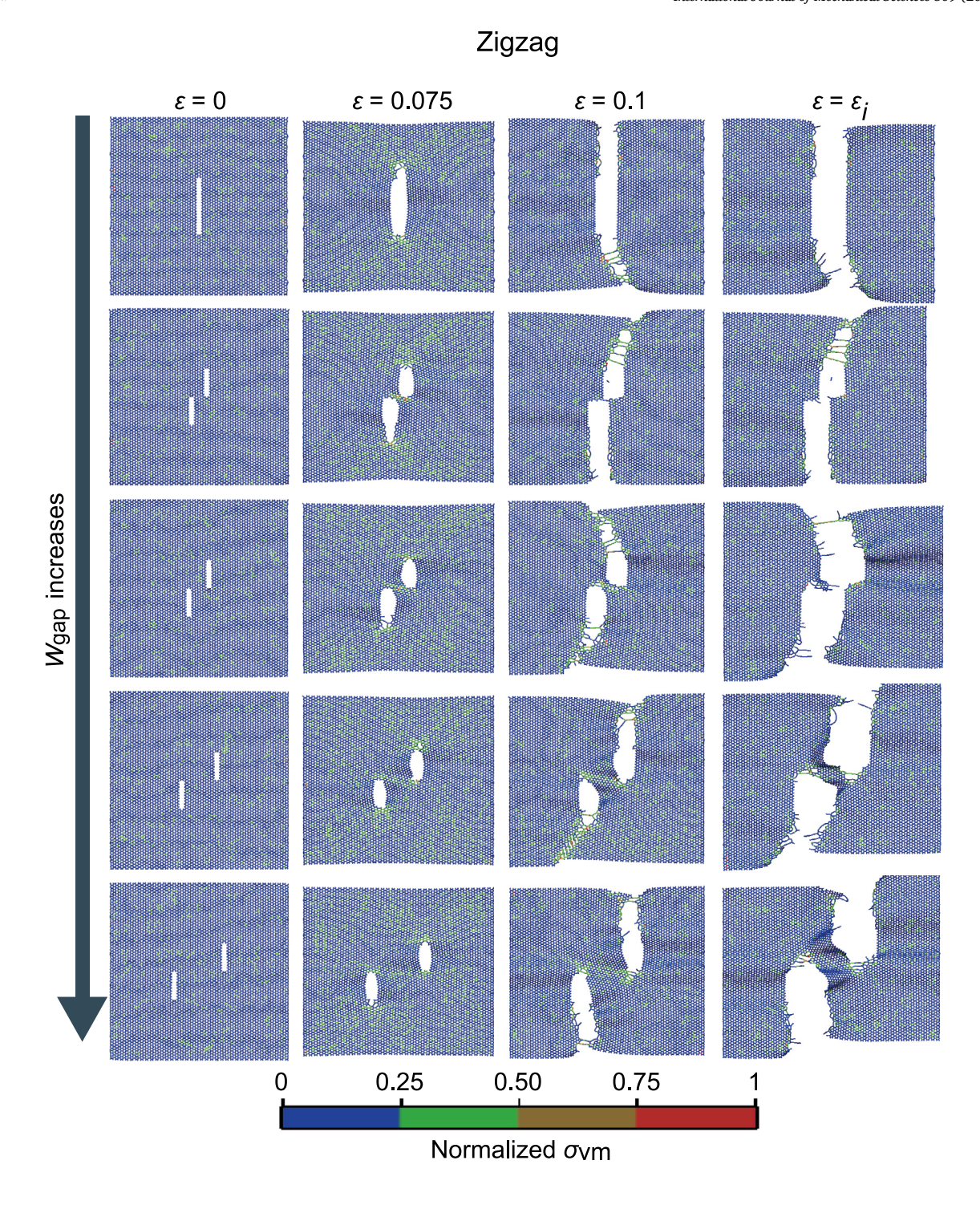


Fig. 7. Snapshots of the ZZ structures (ZZ1 to 5) at certain values of tensile strain. Rows display structures with increasing $W_{\rm gap}=0,1.276,1.701,2.978$, and 4.254 nm, from top to bottom. Columns display structures with strain values, from left to right, corresponding to $\varepsilon=0,0.075,0.1$ and a specific value named " ε_i ". This last one was chosen according to the fracture behavior of each structure. From top to bottom: $\varepsilon_i=0.17,0.12,0.215,0.2$ and 0.2. The color code corresponding to the scale of von Mises stresses, $\sigma_{\rm vm}$, is shown below the figures.

feature on the structure frames corresponding to $\epsilon=0.075$ is the concentration of stresses at the regions between the cracks and lateral extremities of the systems, and at the regions between the cracks. However, for structures exhibiting low $W_{\rm gap}$ values, the region between the cracks undergoes rapid coalescence, thereby enlarging the area of the cracks and decreasing the total stress of these structures. In the case of structures exhibiting large values of $W_{\rm gap}$, the region between the

cracks does not break, but rather exhibits undulations, thereby giving rise to the "lever"-like behavior. The regions between the crack and the lateral extremities continue to undergo stress, causing the stress-curve to rise.

Finally, it is worth to mention that the fracture strain also increases with $W_{\rm gap}$. Due to non-zero residual stresses that are computed due to thermal fluctuations, the value of 1 GPa has been established as

Table 4 Stress intensity factor K_{IC} .

	• 10		
Case	2a ₀ (nm)	$K_{\rm IC} \ ({\rm MPa}\sqrt{\rm m})$	Averaged K_{IC} (MPa \sqrt{m})
AC1	5.388	7.291	_
AC6	2.410	5.961	_
-	-	-	6.626
ZZ1	5.281	6.038	_
ZZ6	2.333	5.386	_
_	_	_	5.712

the stress value below which the structure is deemed fractured for the purpose of determining the rupture strain and calculations of toughness.

3.2. Design of crack geometry

Fig. 5(d) shows an approximately linear increase of the peak stress σ_p with the crack gap width, $W_{\rm gap}$. Based on that, we propose a new, more general relationship between σ_p and $W_{\rm gap}$, given by:

$$\sigma_p = \sigma_p \left(a^{\text{eff}}, W_{\text{gap}} \right) = \frac{K_{\text{IC}}}{\sqrt{\pi a^{\text{eff}}}} \left(1 + \alpha W_{\text{gap}} \right), \tag{7}$$

where $K_{\rm IC}$ is the critical stress intensity factor of graphene with a single crack, and α is a regression coefficient obtained from simulation data varying with $W_{\rm gap}$ for a fixed value of $a_{\rm eff}$. Eq. (7) shows the new relationship between the peak stress and the crack gap width and effective half crack length. In this expression, we assume that the inner and outer crack tips are subjected to the same stress intensity factor. This allows the pair of cracks to be represented by a single effective value that approximates the overall fracture-driving effect. While this homogenization does not capture tip-specific variations, it provides a practical means to correlate the peak stress with $W_{\rm gap}$, and it remains consistent with the fracture behaviors observed in our atomistic simulations. To validate this relationship, additional simulations are needed for structures with different values of effective crack length. They are carried out with structures possessing $2a_1 = 1.347$ nm in the armchair direction (AC6 to 8) and $2a_1 = 1.351$ nm in the zigzag direction (structures ZZ6 to 8). The averaged $K_{\rm IC}$ for each chirality obtained using Eq. (5) and σ_p for each value of a_0 , are listed in Table 4. With the results from the simulations, the regression coefficient α can be obtained for each value of $2a_1$.

The excellent agreement between the analytical predictions of peak stress based on Eq. (7) alongside the simulation results, is shown in Fig. 8. It demonstrates that $W_{\rm gap}$ can be tuned to enhance the peak stress. The graph would be symmetric with respect to the *y*-axis. The linear model proposed in Eq. (7) will not be valid for large values $W_{\rm gap}$, since it predicts that the peak stress can overpass both the theoretical maximum, given by $K_{\rm IC}/\sqrt{\pi(0.5a^{\rm eff})}$, and that of pristine graphene (dotted lines in Fig. 8). Our model is interpreted as the linear approximation of the dependence of the peak stress on $W_{\rm gap}$. Eq. (7) remains valid for crack gaps up to an upper bound $W_{\rm gap}^{\rm lim}$ expressed as

$$W_{\rm gap}^{\rm lim} = \frac{\sqrt{2} - 1}{\alpha},\tag{8}$$

derived by equating the peak stress for two cases: $\sigma_p \left(0.5a^{\rm eff}, W_{\rm gap} = 0\right) = \sigma_p \left(a^{\rm eff}, W_{\rm gap} \gg 1\right)$. Table 5 shows $W_{\rm gap}^{\rm lim}$ corresponding to $2a_1$ for armchair and zigzag, respectively.

This upper bound should be regarded as the mathematical limit of the linear approximation in Eq. (7). At the same time, because it coincides with the condition where the dual-crack system becomes equivalent to a reference single crack, it may also be viewed as an estimate of the physical spacing beyond which crack—crack interactions are no longer significant.

Another interesting result can be inferred from Fig. 8. The coefficient α that determines the linear dependence of σ_p on $W_{\rm gap}$ decreases

Table 5 Design limit of crack gap $W_{\rm gap}^{\rm lim}$ as a function of crack length $2a_1$.

Type	2 <i>a</i> ₁ (nm)	$\alpha \left(\mathrm{nm}^{-1} \right)$	$W_{\rm gap}^{\rm lim}$ (nm)
AC	1.347	0.045	9.205
AC	2.836	0.036	11.506
ZZ	1.351	0.024	17.259
ZZ	2.825	0.055	7.531

Table 6 Fracture behavior of graphene structures as $W_{\rm gap}$ increases.

Case	$W_{ m gap}$	Fracture mode	Case	$W_{ m gap}$	Fracture behavior
AC1	0	Single crack	ZZ1	0	Single crack
AC2	1.228	Coalescence	ZZ2	1.276	Coalescence
AC3	1.719	Coalescence	ZZ3	1.701	Coalescence
AC4	2.947	Lever	ZZ4	2.978	Lever
AC5	4.175	Lever	ZZ5	4.254	Lever

with increasing $2a_1$ for armchair, and increases with increasing $2a_1$ for zigzag structures. This means that the dependence of the peak stress on $W_{\rm gap}$ behaves in an opposite way between the ZZ and AC structures.

3.3. Fracture analysis

The fracture of graphene structures in this study can be classified into three types, based on $W_{\rm gap}$: single crack propagation, crack coalescence, and separate crack propagation followed by full rupture designated as *lever* behavior. The structures and their corresponding fracture behaviors are listed in Table 6. Crack coalescence is defined as the crack connection between two already existing parallel cracks. As seen in Figs. 6 and 7, when $W_{\rm gap}$ increases, the fracture mode converts from crack coalescence to lever behavior.

Further insights into the fracture behavior are provided in Fig. 9. It shows the atomic configurations near the crack tips at various strain values for both armchair and zigzag graphene structures. Two groups of carbon atoms, colored orange and yellow, are selected to be tracked during the tensile strain. The purpose is to see how the crack coalescence starts and propagates in each type of structure/chirality. For both chiralities, we observe that crack coalescence initiates from the tips of the previous cracks and progresses toward the center region as strain increases, particularly for intermediate values of $W_{\mathrm{gap}}.$ In the case of the armchair structure with $W_{\rm gap} = 1.719$ nm (Fig. 9(a)), the local atomic arrangement exhibits a gradual shear-like distortion prior to coalescence, indicating one kind of a progressive failure mechanism. On the other hand, the zigzag structure (Fig. 9(b)) with a comparable $W_{\rm gap}$, exhibits more dilative deformation followed by localized and less progressive bond breaking, which is consistent with the lower fracture toughness observed in zigzag graphene.

Figs. 9(c) and 9(e) show examples of the region between the cracks for AC and ZZ structures, respectively, corresponding to values of $W_{\rm gap} \sim 2.9$ nm. For these structures, the formation of wide "levers" is clearly evident in the respective fourth rows of Figs. 6 and 7. In both cases, the fracture process occurs first by the crack propagation from the cracks to the lateral extremities. Subsequently, the process advances through the tearing of the carbon bonds at the edges of the lever, along the diagonal direction of the structure. Furthermore, a subtle yet substantial qualitative distinction emerges between the coalescence observed in armchair (AC) and zigzag (ZZ) structures, as evidenced by Figs. 9(a), 9(b) and 9(d). In the AC structure with a small $W_{\rm gap}$, (see Fig. 9(a)), the bond breaking occurs precisely along the zigzag line connecting the extremities of the existing cracks. In the ZZ structures depicted in Figs. 9(b) and 9(d), the bond breaking occurs along a zigzag line, accompanied by a minor "lever"-like deformation of the region between the cracks and the formation of carbon chains, which happen even for the ZZ structure with the smallest value of $W_{\rm gap}$ (see Fig. 9(d)).

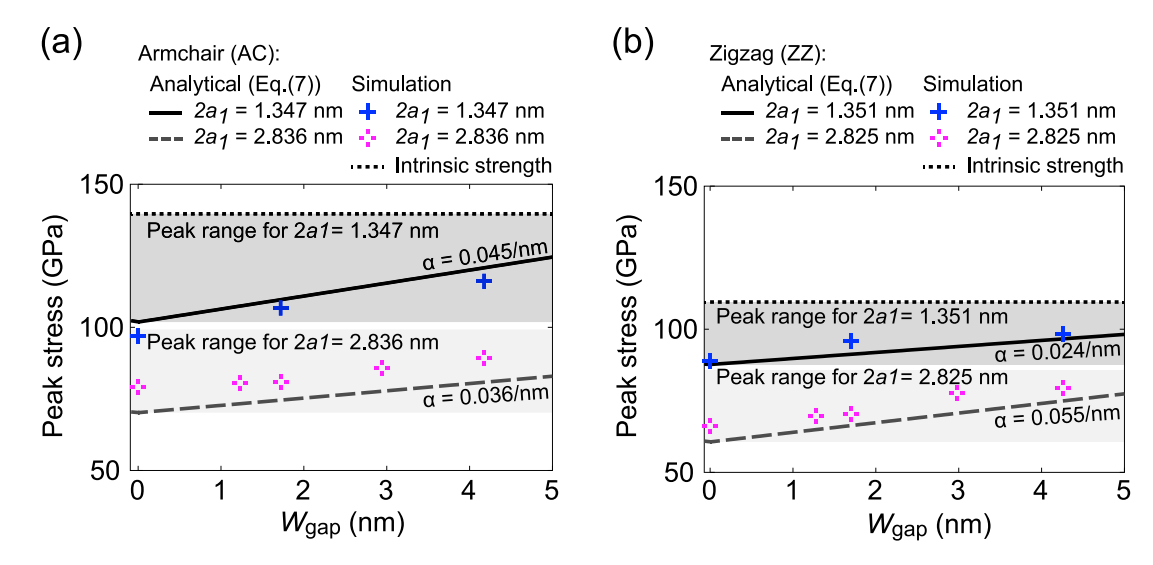


Fig. 8. Peak stress versus W_{gap} for the graphene with each crack length $2a_1$ in (a) armchair and (b) zigzag. The dark and light gray colored regions indicate the range of the possible peak stress for each value of $2a_1$. The value α is calculated for each crack length $2a_1$.

Table 7
Propagation time of outer and inner crack tips (Δt_{outer} and Δt_{inner}) as a function of W_{gap} for armchair and zigzag cases.

Case	W _{gap} (nm)	$\Delta t_{ m outer}$ (ns)	Δt _{inner} (ns)	Case	W _{gap} (nm)	$\Delta t_{ m outer}$ (ns)	Δt _{inner} (ns)
AC1	0	2.35	-	ZZ1	0	0.95	_
AC2	1.228	2.90	0.75	ZZ2	1.276	1.1	0.45
AC3	1.719	2.20	1.10	ZZ3	1.701	1.60	1.55
AC4	2.947	1.80	4.05	ZZ4	2.978	1.05	4.60
AC5	4.175	2.05	11	ZZ5	4.254	0.50	5.00

The third and fourth columns of Figs. 6 and 7 offer insight into the brittle-to-ductile transition phenomenon. At $\varepsilon\sim0.1$, for smaller values of $W_{\rm gap}$, the rupture of the structures occurs concurrently at both the lateral edges of the entire structure and between the cracks. In this particular instance, the observed fracture mode is *coalescence*. In the case of $\varepsilon\sim0.1$ and larger values of $W_{\rm gap}$, the rupture of the structures occurs at the lateral edges first, much before the break of the region between the cracks. The width of the preexisting cracks increases, but the region between them becomes loose and flexible, giving rise to the "lever"-like region and the corresponding fracture mode.

Notably, in both structures, the deformation patterns suggest that the crack tips act as localized stress concentrators where atomic bond rotation and stretching precede rupture. As the strain increases, the transition from elastic deformation to crack propagation becomes visible through increased atomic displacement and asymmetry around the crack front. These visualizations support the interpretation of the lever behavior observed in larger $W_{\rm gap}$ structures, where the region between cracks deforms out-of-plane, allowing the structure to sustain additional strain before failure. Therefore, Fig. 9 provides atomistic evidence supporting the shift in fracture mode from brittle (coalescence) to ductile-like (lever) as $W_{\rm gap}$ increases.

To quantify the fracture kinetics, we evaluated the time required for outer crack tips to propagate and for inner cracks to coalesce at different $W_{\rm gap}$ values (new Fig. 10 and new Table 7). In the coalescence regime ($W_{\rm gap}\approx 1.2$ –1.7 nm), the inner tips merged within 0.75–1.1 ns for armchair and for 0.45–1.55 ns for zigzag, significantly earlier than the corresponding outer-tip propagation times of 2.2–2.9 ns and 1.1–1.6 ns, respectively. This indicates that crack coalescence accelerates the fracture process, leading to rapid failure. At comparatively large spacings ($W_{\rm gap} \geq 2.9$ nm), the fracture mechanism transitions. The inner cracks required 4.05–11 ns for armchair and 4.6–5 ns for zigzag to merge, while the outer cracks fractured within 1.8–2.05 ns and 0.5–1.05 ns,

respectively. In this regime, the cracks propagate independently, and the intervening ligament undergoes progressive out-of-plane rotation and tearing rather than immediate inner-tip coalescence. The ligament acts as a hinge or lever, dissipating strain energy gradually before final rupture. This lever-type behavior substantially reduces the effective crack-tip velocity, delays fracture, and promotes a more damage-tolerant response. The transition between the two regimes occurs at intermediate spacings ($W_{\rm gap} \sim 1.7$ –2.9 nm) and is consistently observed for both armchair and zigzag chiralities.

Beyond categorizing the fracture behaviors, it is also instructive to consider their potential implications for material design. The three observed modes — single crack propagation, crack coalescence, and separate crack propagation (lever-type behavior) - offer distinct mechanical characteristics. Single crack propagation typically results in abrupt brittle failure, but its predictability may be advantageous when controlled fracture paths are required, for example in nanoscale patterning or deliberate weakening of predefined regions. Crack coalescence, although reducing strength due to the amplification of stresses at the inner tips, could be exploited to localize fracture initiation or to facilitate controlled energy release. In contrast, separate crack propagation at larger spacings enables the ligament between cracks to deform in a lever-like manner, delaying catastrophic rupture and enhancing energy absorption. This ductile-like response provides a pathway for designing two-dimensional materials with improved toughness and damage tolerance.

4. Conclusions

This study investigates the fracture behavior of graphene structures with preexisting parallel cracks, focusing on the influence of crack spacing and chirality under tensile strain. Molecular dynamics simulations revealed that crack coalescence occurs at smaller $W_{\rm gap}$, leading to a significant reduction in strength. Stress–strain curves demonstrate

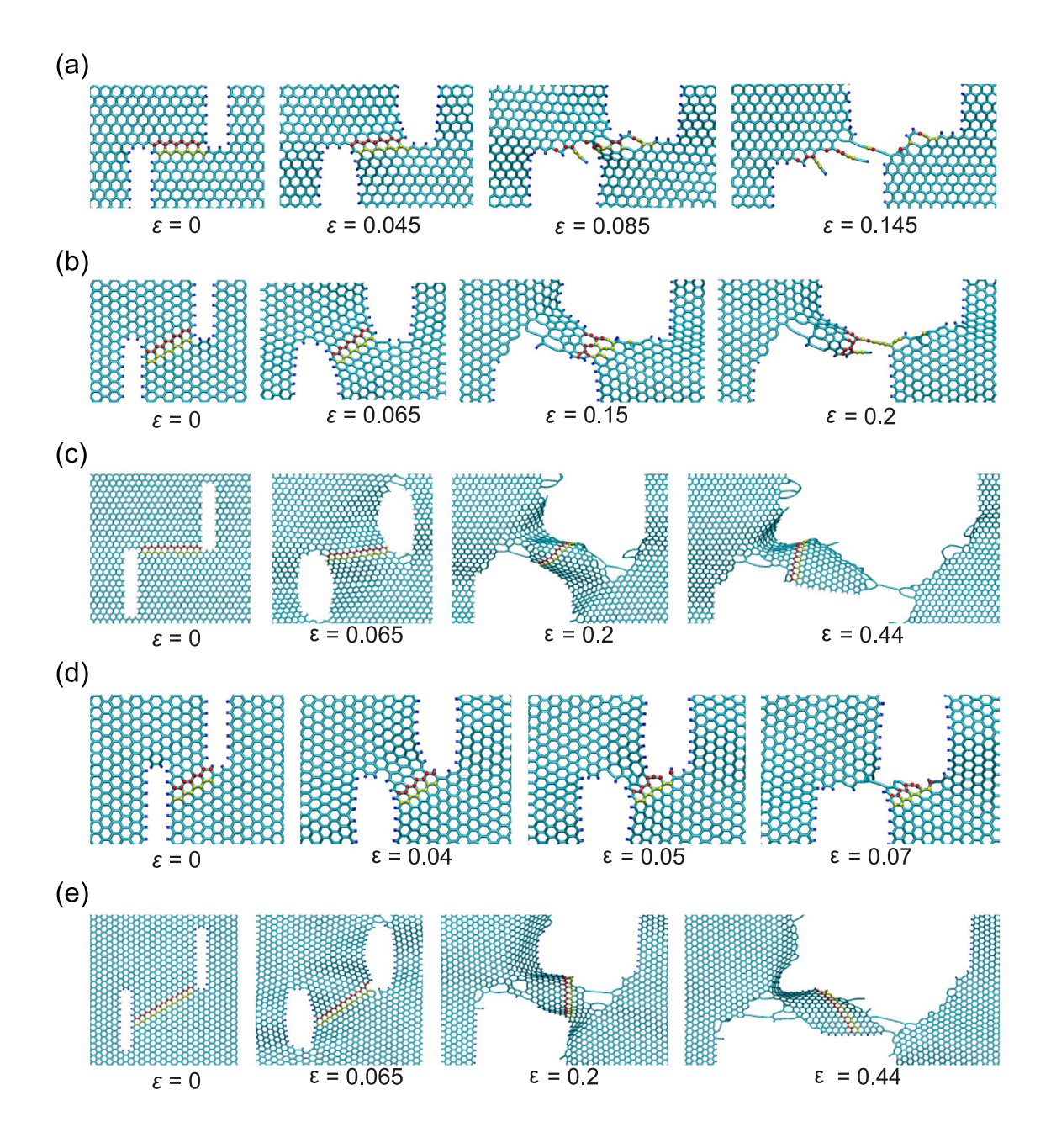
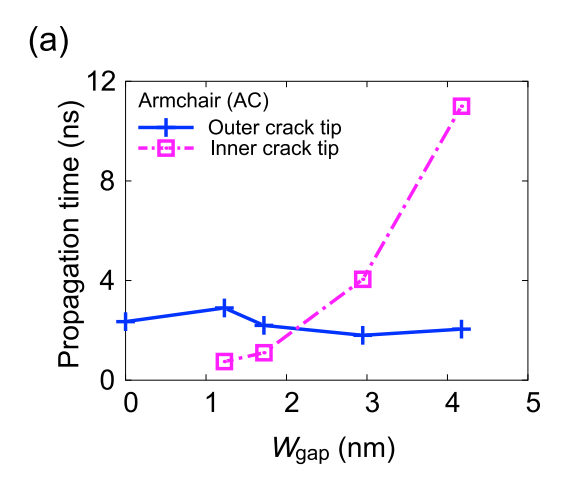


Fig. 9. Atomic configurations near crack tips for armchair and zigzag cases: (a) AC3 with a crack gap $W_{\rm gap}=1.719$ nm. (b) ZZ3 with $W_{\rm gap}=1.701$ nm. (c) AC4 $W_{\rm gap}=2.947$ nm. (d) ZZ2 with $W_{\rm gap}=1.276$ nm. (e) ZZ4 with $W_{\rm gap}=4.254$ nm. Red and yellow atoms show the zigzag direction in each structure. Armchair has a crack length of $2a_1=2.836$ nm and crack width of 2b=0.614 nm, and zigzag has $2a_1=2.825$ nm, 2b=0.567 nm, respectively.

an upward shift as the gap between cracks $W_{\rm gap}$ increases, indicating a higher peak stress and a tendency for crack coalescence when the crack distances are small. Crack coalescence is observed when $W_{\rm gap}$ is below a specific threshold, leading to a significant deterioration in the strength of the material. For larger crack separations, independent crack propagation occurs, with the material exhibiting ductile behavior due to a "lever" kind of distortion mechanism, highlighting the transition from brittle to ductile fracture as the crack gap increases. The study also establishes that effective stress intensity factors increase with the gap size, further indicating the correlation between crack geometry and the mechanical properties of graphene. Then, the design

guidelines for the length and gap of parallel cracks are discussed to predict the peak stress based on the crack geometry. Overall, the results suggest that the geometry and distance between cracks play a critical role in determining the fracture behavior of graphene. The findings offer important insights for designing graphene-based materials with controlled fracture properties, which could be crucial for engineering applications that require high mechanical integrity in the presence of defects.

There are some issues that require further investigation. For example, the apparent absence of the dependence with $W_{\rm gap}$ of the absorption energy of ZZ structures for large values of $W_{\rm gap}$, is a point



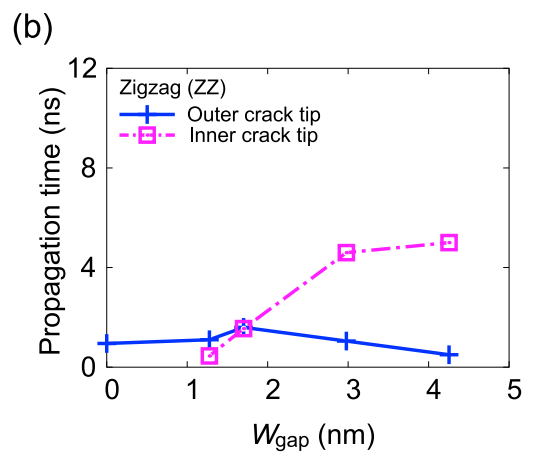


Fig. 10. Propagation time of outer and inner crack tips as a function of $W_{\rm gap}$. Armchair and zigzag configurations are shown in panels (a) and (b), respectively. The time is measured from the onset of crack initiation to complete fracture.

of interest. Extensions of the present investigation to explore the dependence of the primary quantities defined herein on factors such as sample total size, crack size, position and orientation, temperature, polycrystallinity of the samples, and other variables of interest will be the subject of future publications.

CRediT authorship contribution statement

Suyeong Jin: Writing – original draft, Visualization, Methodology, Investigation, Formal analysis, Data curation, Conceptualization. Jung-Wuk Hong: Writing – review & editing, Validation, Supervision, Funding acquisition. Chiara Daraio: Writing – review & editing, Validation, Supervision, Funding acquisition. Alexandre F. Fonseca: Writing – review & editing, Validation, Supervision, Methodology, Data curation, Conceptualization.

Declaration of competing interest

The authors declare that they have no known competing financial interests or personal relationships that could have appeared to influence the work reported in this paper.

Acknowledgments

This work was supported by Basic Science Research Program through the National Research Foundation of Korea (NRF) funded by the Ministry of Education (No. RS-2023-00242455). AFF is a fellow of the Brazilian Agency CNPq-Brazil (#303284/2021-8 and #302009/2025-6) and acknowledges grants #2023/02651-0 and #2024/14403-4 from São Paulo Research Foundation (FAPESP). This work was supported by the Heritage Medical Research Institute (HMRI) at Caltech and the National Science Foundation, Center to Stream Healthcare in Place (C2SHIP), Award No. 2052827 (C.D.). Computational resources were provided by the High-Performance Computing Center at Caltech, the Coaraci Supercomputer (FAPESP grant #2019/17874-0) and the Center for Computing in Engineering and Sciences at Unicamp (FAPESP grant #2013/08293-7).

Data availability

Data will be made available on request.

References

- [1] Novoselov KS, Geim AK, Morozov SV, Jiang D, Zhang Y, Dubonos SV, Grigorieva IV, Firsov AA. Electric field effect in atomically thin carbon films. Science 2004;306(5696):666–9. http://dx.doi.org/10.1126/science.1102896.
- [2] Castro Neto AH, Guinea F, Peres NMR, Novoselov KS, Geim AK. The electronic properties of graphene. Rev Modern Phys 2009;81:109–62. http://dx.doi.org/10. 1103/RevModPhys.81.109.
- [3] Zhang P, Ma L, Fan F, Zeng Z, Peng C, Loya PE, Liu Z, Gong Y, Zhang J, Zhang X, Ajayan PM, Zhu T, Lou J. Fracture toughness of graphene. Nat Commun 2014;5(1):3782. http://dx.doi.org/10.1038/ncomms4782.
- [4] Papageorgiou DG, Kinloch IA, Young RJ. Mechanical properties of graphene and graphene-based nanocomposites. Prog Mater Sci 2017;90:75–127. http://dx.doi. org/10.1016/j.pmatsci.2017.07.004.
- [5] Lee C, Wei X, Kysar JW, Hone J. Measurement of the elastic properties and intrinsic strength of monolayer graphene. Science 2008;321(5887):385–8. http: //dx.doi.org/10.1126/science.1157996.
- [6] Li X, Cai W, An J, Kim S, Nah J, Yang D, Piner R, Velamakanni A, Jung I, Tutuc E, Banerjee SK, Colombo L, Ruoff RS. Large-area synthesis of high-quality and uniform graphene films on copper foils. Science 2009;324(5932):1312–4. http://dx.doi.org/10.1126/science.1171245.
- [7] Levendorf MP, Ruiz-Vargas CS, Garg S, Park J. Transfer-free batch fabrication of single layer graphene transistors. Nano Lett 2009;9(12):4479–83. http://dx.doi. org/10.1021/nl902790r.
- [8] Yu Q, Lian J, Siriponglert S, Li H, Chen YP, Pei S-S. Graphene segregated on ni surfaces and transferred to insulators. Appl Phys Lett 2008;93(11):113103. http://dx.doi.org/10.1063/1.2982585.
- [9] Lin L, Zhang J, Su H, Li J, Sun L, Wang Z, Xu F, Liu C, Lopatin S, Zhu Y, Jia K, Chen S, Rui D, Sun J, Xue R, Gao P, Kang N, Han Y, Xu HQ, Cao Y, Novoselov KS, Tian Z, Ren B, Peng H, Liu Z. Towards super-clean graphene. Nat Commun 2019;10(1):1912. http://dx.doi.org/10.1038/s41467-019-09565-4.
- [10] Bøggild P. Research on scalable graphene faces a reproducibility gap. Nat Commun 2023;14(1):1126. http://dx.doi.org/10.1038/s41467-023-36891-5.
- [11] Amontree J, Yan X, DiMarco CS, Levesque PL, Adel T, Pack J, Holbrook M, Cupo C, Wang Z, Sun D, Biacchi AJ, Wilson-Stokes CE, Watanabe K, Taniguchi T, Dean CR, Hight Walker AR, Barmak K, Martel R, Hone J. Reproducible graphene synthesis by oxygen-free chemical vapour deposition. Nature 2024;630(8017):636–42. http://dx.doi.org/10.1038/s41586-024-07454-5.
- [12] Pham PV, Mai T-H, Dash SP, Biju V, Chueh Y-L, Jariwala D, Tung V. Transfer of 2d films: From imperfection to perfection. ACS Nano 2024;18(23):14841–76. http://dx.doi.org/10.1021/acsnano.4c00590.
- [13] Grantab R, Shenoy VB, Ruoff RS. Anomalous strength characteristics of tilt grain boundaries in graphene. Science 2010;330(6006):946–8. http://dx.doi.org/10. 1126/science.1196893.
- [14] Zhang T, Li X, Kadkhodaei S, Gao H. Flaw insensitive fracture in nanocrystalline graphene. Nano Lett 2012;12(9):4605–10. http://dx.doi.org/10.1021/nl301908b.
- [15] López-Polín G, Gómez-Herrero J, Gómez-Navarro C. Confining crack propagation in defective graphene. Nano Lett 2015;15(3):2050–4. http://dx.doi.org/10.1021/ nl504936q.
- [16] Meng F, Chen C, Song J. Dislocation shielding of a nanocrack in graphene: Atomistic simulations and continuum modeling. J Phys Chem Lett 2015;6(20):4038–42. http://dx.doi.org/10.1021/acs.jpclett.5b01815.
- [17] Mostério NCB, Fonseca AF. Thermal expansion behavior of holes in graphene nanomeshes. Phys Rev B 2014;89:195437. http://dx.doi.org/10.1103/PhysRevB. 89.195437.

- [18] Chen Y, Wang Y, Zhu S, Fu K, Han X, Wang Y, Zhao B, Li T, Liu B, Li Y, Dai J, Xie H, Li T, Connell JW, Lin Y, Hu L. Nanomanufacturing of graphene nanosheets through nano-hole opening and closing. Mater Today 2019;24:26–32. http://dx.doi.org/10.1016/j.mattod.2018.09.001.
- [19] Yang Z, Wang R, Li H, Tang H-K, Han K. Phonon thermal transport in polycrystalline graphene:effects of grain, vacancy and strain. Int J Heat Mass Transfer 2023;209:124057. http://dx.doi.org/10.1016/j.ijheatmasstransfer.2023.124057.
- [20] Hinnefeld JH, Gill ST, Zhu S, Swanson WJ, Li T, Mason N. Reversible mechanical and electrical properties of ripped graphene. Phys Rev Appl 2015;3:014010. http://dx.doi.org/10.1103/PhysRevApplied.3.014010.
- [21] Mulla R, White AO, Dunnill CW, Barron AR. The role of graphene in new thermoelectric materials. Energy Adv 2023;2:606–14. http://dx.doi.org/10.1039/ D3YA00085K.
- [22] Dewapriya M, Meguid S. Atomistic simulations of nanoscale crack-vacancy interaction in graphene. Carbon 2017;125:113–31. http://dx.doi.org/10.1016/j. carbon.2017.09.015.
- [23] Dewapriya M, Meguid S, Rajapakse R. Atomistic modelling of crack-inclusion interaction in graphene. Eng Fract Mech 2018;195:92–103. http://dx.doi.org/ 10.1016/j.engfracmech.2018.04.003.
- [24] Dewapriya M, Meguid S. Tailoring fracture strength of graphene. Comput Mater Sci 2018;141:114–21. http://dx.doi.org/10.1016/j.commatsci.2017.09.005.
- [25] Yao J, Xia Y, Dong S, Yu P, Zhao J. Finite element analysis and molecular dynamics simulations of nanoscale crack-hole interactions in chiral graphene nanoribbons. Eng Fract Mech 2019;218:106571. http://dx.doi.org/10.1016/j. engfracmech.2019.106571.
- [26] Brodnik NR, Brach S, Long CM, Ravichandran G, Bourdin B, Faber KT, Bhat-tacharya K. Fracture diodes: Directional asymmetry of fracture toughness. Phys Rev Lett 2021;126:025503. http://dx.doi.org/10.1103/PhysRevLett.126.025503.
- [27] Felix LC, Galvao DS. Guided fractures in graphene mechanical diode-like structures. Phys Chem Chem Phys 2022;24:13905–10. http://dx.doi.org/10.1039/D2CP01207C.
- [28] Gamboa-Suárez A, Seuret-Hernández HY, Leyssale J-M. Mechanical properties of pristine and nanocrystalline graphene up to ultra-high temperatures. Carbon Trends 2022;9:100197. http://dx.doi.org/10.1016/j.cartre.2022.100197.
- [29] Thompson AP, Aktulga HM, Berger R, Bolintineanu DS, Brown WM, Crozier PS, in 't Veld PJ, Kohlmeyer A, Moore SG, Nguyen TD, Shan R, Stevens MJ, Tranchida J, Trott C, Plimpton SJ. Lammps a flexible simulation tool for particle-based materials modeling at the atomic, meso, and continuum scales. Comput Phys Comm 2022;271:108171. http://dx.doi.org/10.1016/j.cpc.2021. 108171.
- [30] van Duin ACT, Dasgupta S, Lorant F, Goddard WA. Reaxff: A reactive force field for hydrocarbons. J Phys Chem A 2001;105(41):9396–409. http://dx.doi.org/10. 1021/in004368u
- [31] Brenner DW, Shenderova OA, Harrison JA, Stuart SJ, Ni B, Sinnott SB. A second-generation reactive empirical bond order (rebo) potential energy expression for hydrocarbons. J Phys: Condens Matter 2002;14(4):783. http://dx.doi.org/10.1088/0953-8984/14/4/312.
- [32] Stuart SJ, Tutein AB, Harrison JA. A reactive potential for hydrocarbons with intermolecular interactions. J Chem Phys 2000;112(14):6472–86. http://dx.doi. org/10.1063/1.481208.
- [33] Yakobson BI, Brabec CJ, Bernholc J. Nanomechanics of carbon tubes: Instabilities beyond linear response. Phys Rev Lett 1996;76:2511–4. http://dx.doi.org/10. 1103/PhysRevLett.76.2511.
- [34] Wei C, Srivastava D, Cho K. Thermal expansion and diffusion coefficients of carbon nanotube-polymer composites. Nano Lett 2002;2(6):647–50. http://dx. doi.org/10.1021/nl025554+.
- [35] Srivastava D, Wei K, Cho C. Nanomechanics of carbon nanotubes and composites. Appl Mech Rev 2003;56(2):215–30. http://dx.doi.org/10.1115/1.1538625.
- [36] Neek-Amal M, Peeters FM. Lattice thermal properties of graphane: Thermal contraction. Rough Heat Capacit Phys Rev B 2011;83:235437. http://dx.doi.org/ 10.1103/PhysRevB.83.235437.
- [37] Muniz AR, Fonseca AF. Carbon-based nanostructures derived from bilayer graphene with zero thermal expansion behavior. J Phys Chem C 2015;119(30):17458-65. http://dx.doi.org/10.1021/acs.jpcc.5b05602.
- [38] Zhao H, Aluru NR. Temperature and strain-rate dependent fracture strength of graphene. J Appl Phys 2010;108(6):064321. http://dx.doi.org/10.1063/1. 3488620.
- [39] Jhon YI, Jhon YM, Yeom GY, Jhon MS. Orientation dependence of the fracture behavior of graphene. Carbon 2014;66:619–28. http://dx.doi.org/10.1016/j.carbon.2013.09.051.
- [40] Jung G, Qin Z, Buehler MJ. Molecular mechanics of polycrystalline graphene with enhanced fracture toughness. Extrem Mech Lett 2015;2:52–9. http://dx. doi.org/10.1016/j.eml.2015.01.007.

- [41] Chen M, Quek S, Sha Z, Chiu C, Pei Q, Zhang Y. Effects of grain size, temperature and strain rate on the mechanical properties of polycrystalline graphene – a molecular dynamics study. Carbon 2015;85:135–46. http://dx.doi.org/10.1016/ i.carbon.2014.12.092.
- [42] Yin H, Qi HJ, Fan F, Zhu T, Wang B, Wei Y. Griffith criterion for brittle fracture in graphene. Nano Lett 2015;15(3):1918–24. http://dx.doi.org/10.1021/ n15047686
- [43] Shekhawat A, Ritchie RO. Toughness and strength of nanocrystalline graphene. Nat Commun 2016;7(1):10546. http://dx.doi.org/10.1038/ncomms10546.
- [44] Budarapu PR, Javvaji B, Sutrakar VK, Mahapatra DR, Paggi M, Zi G, Rabczuk T. Lattice orientation and crack size effect on the mechanical properties of graphene. Int J Fract 2017;203(1):81–98. http://dx.doi.org/10.1007/s10704-016-0115-9.
- [45] Lee S, Pugno NM, Ryu S. Atomistic simulation study on the crack growth stability of graphene under uniaxial tension and indentation. Meccanica 2019;54(13):1915–26. http://dx.doi.org/10.1007/s11012-019-01027-x.
- [46] Fonseca AF, Galvão DS. Self-tearing and self-peeling of folded graphene nanoribbons. Carbon 2019;143:230–9. http://dx.doi.org/10.1016/j.carbon.2018. 11.020.
- [47] Ma J, Wang K, Tang M, He Y, Gao X, Gao P, Sun J. Effect of monovacancy defects on anisotropic mechanical behavior of monolayer graphene: A molecular dynamics study. Diam Relat Mater 2024;148:111437. http://dx.doi.org/10.1016/ j.diamond.2024.111437.
- [48] Tangarife E, Gonzalez R, Cardenas C, Bringa E, Munoz F. Molecular simulations of carbon allotropes in processes with creation and destruction of chemical bonds. Carbon 2019;144:177–84. http://dx.doi.org/10.1016/j.carbon.2018.11. 081.
- [49] de Sousa J, Brunetto G, Coluci V, Galvão D. Torsional superplasticity of graphyne nanotubes. Carbon 2016;96:14–9. http://dx.doi.org/10.1016/j.carbon.2015.09. 039.
- [50] De Sousa J, Bizao R, Sousa Filho V, Aguiar A, Coluci V, Pugno N, Girao E, Souza Filho A, Galvao D. Elastic properties of graphyne-based nanotubes. Comput Mater Sci 2019;170:109153. http://dx.doi.org/10.1016/j.commatsci.2019.109153.
- [51] Brandão WHS, Aguiar AL, Ribeiro LA, Galvão DS, De Sousa JM. On the mechanical properties of popgraphene-based nanotubes: a reactive molecular dynamics study. ChemPhysChem 2021;22(7):701–7. http://dx.doi.org/10.1002/ cphc.202000840.
- [52] Nair AK, Cranford SW, Buehler MJ. The minimal nanowire: Mechanical properties of carbyne. Europhys Lett 2011;95(1):16002. http://dx.doi.org/10.1209/0295-5075/95/16002.
- [53] Brandão W, De Sousa J, Aguiar A, Galvão D, Ribeiro LA, Fonseca AF. First-principles and reactive molecular dynamics study of the elastic properties of pentahexoctite-based nanotubes. Mech Mater 2023;183:104694. http://dx.doi.org/10.1016/j.mechmat.2023.104694.
- [54] de Sousa JM, Botari T, Perim E, Bizao RA, Galvao DS. Mechanical and structural properties of graphene-ike carbon nitride sheets. RSC Adv 2016;6:76915–21. http://dx.doi.org/10.1039/C6RA14273G.
- [55] Roman RE, Cranford SW. Defect sensitivity and weibull strength analysis of monolayer silicene. Mech Mater 2019;133:13–25. http://dx.doi.org/10.1016/j. mechmat.2019.01.014.
- [56] Shishir MIR, Elapolu MSR, Tabarraei A. Investigation of fracture and mechanical properties of monolayer c3n using molecular dynamic simulations. Mech Mater 2021;160:103895. http://dx.doi.org/10.1016/j.mechmat.2021.103895.
- [57] Chenoweth K, van Duin ACT, Goddard WA. Reaxff reactive force field for molecular dynamics simulations of hydrocarbon oxidation. J Phys Chem A 2008;112(5):1040–53. http://dx.doi.org/10.1021/jp709896w.
- [58] Medhekar NV, Ramasubramaniam A, Ruoff RS, Shenoy VB. Hydrogen bond networks in graphene oxide composite paper: Structure and mechanical properties. ACS Nano 2010;4(4):2300–6. http://dx.doi.org/10.1021/nn901934u.
- [59] Bu Y, Li K, Guo F, Liang Z, Zhang J. Mechanical behavior and failure mechanism of multilayer graphene oxides with various oxygen contents and functional types: A reaxff molecular dynamics simulation. Appl Surf Sci 2022;606:154920. http://dx.doi.org/10.1016/j.apsusc.2022.154920.
- [60] Bidhendi MRT, Behdinan K. High-velocity transverse impact of monolayer graphene oxide by a molecular dynamics study. Comput Mater Sci 2023;216:111881. http://dx.doi.org/10.1016/j.commatsci.2022.111881.
- [61] Desyatkin VG, Martin WB, Aliev AE, Chapman NE, Fonseca AF, Galvão DS, Miller ER, Stone KH, Wang Z, Zakhidov D, Limpoco FT, Almahdali SR, Parker SM, Baughman RH, Rodionov VO. Scalable synthesis and characterization of multi-layer γ-graphyne, new carbon crystals with a small direct band gap. J Am Chem Soc 2022:144(39):17999–8008. http://dx.doi.org/10.1021/jacs.2c06583.
- [62] Barrett TJ, Minus ML. Nosé-hoover integrators at-a-glance: Barostat integration has a demonstrable effect on uniaxial tension results of solid materials. J Chem Theory Comput 2025;21(2):517–29. http://dx.doi.org/10.1021/acs.jctc.4c01190.

- [63] Schneider T, Stoll E. Molecular-dynamics study of a three-dimensional onecomponent model for distortive phase transitions. Phys Rev B 1978;17:1302–22. http://dx.doi.org/10.1103/PhysRevB.17.1302.
- [64] Mises Rv. Mechanik der festen k\u00f6rper im plastisch-deformablen zustand, Nachrichten von der Gesellschaft der Wissenschaften zu G\u00f6ttingen. Mathematisch-Physikalische Kl 1913;1913:582–92.
- [65] Fujihara M, Inoue R, Kurita R, Taniuchi T, Motoyui Y, Shin S, Komori F, Maniwa Y, Shinohara H, Miyata Y. Selective formation of zigzag edges in graphene cracks. ACS Nano 2015;9(9):9027–33. http://dx.doi.org/10.1021/ acsnano.5b03079.
- [66] Le M-Q, Batra RC. Mode-i stress intensity factor in single layer graphene sheets. Comput Mater Sci 2016;118:251–8. http://dx.doi.org/10.1016/j.commatsci. 2016.03.027.
- [67] Hwangbo Y, Lee C-K, Kim S-M, Kim J-H, Kim K-S, Jang B, Lee H-J, Lee S-K, Kim S-S, Ahn J-H, Lee S-M. Fracture characteristics of monolayer cvd-graphene. Sci Rep 2014;4(1):4439. http://dx.doi.org/10.1038/srep04439.